doi: 10.32131/jes.6.3

Journal of the Earth Simulator, Volume 6, October 2006, 3–15

Direct Numerical Simulation of the Neutrally Stratified Turbulent Ekman Boundary Layer

Katsuhiro Miyashita[1], Kaoru Iwamoto[1] and Hiroshi Kawamura[1]*

[1] *Department of Mechanical Engineering, Tokyo University of Science, 2641 Yamazaki, Noda-shi, Chiba, 278-8510 Japan*

(Received March 27, 2006; Revised manuscript accepted May 9, 2006)

Abstract Direct numerical simulations (DNSs) are performed for the turbulent Ekman boundary layer over a smooth surface. The Reynolds numbers Re_f are set to be Re_f = 400, 510, 600, 775, 1140 and 1393 where Re_f is based on the geostrophic wind G, the kinematic viscosity ν and Coriolis parameter f. The simulations of Re_f = 1140 and 1393 have been carried out on the Earth Simulator. In the cases of the higher Reynolds numbers, the mean velocity profiles show good agreement with the experimental data of Caldwell *et al*. (1972) and the DNS data of Coleman (1999). A low-speed large-scale structure is found in the upper region, whereas the well-known streaky structure appears in the vicinity of the wall. This large-scale structure is observed in a motion of a material line. The inclination of this structure does not coincide with the direction of the mean flow velocity. The reason is discussed based upon the motion of a material line whose initial position is horizontal in a vicinity of the wall. In addition, the eddy-viscosity model proposed by Blackadar (1962, 1965) is examined with respect to the obtained DNS data base. The improved model gives good agreement with the results by the present DNS.

Keywords: DNS, Ekman boundary layer, turbulence structure, eddy-viscosity model

1. Introduction

Rotation is one of the factors which affect the planetary boundary layer (PBL). The boundary layer under the effect of the system rotation is called the Ekman boundary layer. The Ekman boundary layer is three-dimensional flow in nature, in which three forces are balanced, i.e., the pressure gradient, viscous and the Coriolis forces.

Many numerical simulations of the turbulent PBL have been performed with the advancement of the computer. One of the major tools in numerical researches on the turbulent PBL is large-eddy simulation (LES) (e.g. Moeng [1], Mason [2], Andrén *et al*. [3] and Lin *et al*. [4]), in which the large-scale motions are directly computed while the effect of the unresolved-scale one is approximated by a sub-grid scale model. Another major approach is Reynolds averaged Navier-Stokes equation (RANS) (e.g. Duynkerke [5] and Andrén [6]), in which mean components are only calculated. One of the advantages of LES and RANS is that flow fields of realistic Reynolds numbers can be calculated. Results from LES and RANS, however, include approximation due to the underlying modeling. We adopt here the technique of another approach, i.e., direct numerical simulation (DNS), all of the relevant scale motions are resolved. Therefore, DNS gives accurate reliable data. In addition, DNS of the turbulent Ekman boundary layer provide fundamental information on the three-dimensional turbulent boundary layer as well as the PBL in order to improve turbulence models in LES and RANS.

Among studies of the Ekman boundary layer, the studies using DNS have barely been performed. Coleman *et al*. [7] performed DNSs of the turbulent Ekman boundary layer with low Reynolds numbers, and found that no horizontal roll vortices appeared under neutral stratification. Coleman *et al*. carried out DNSs on buoyantly stable [8] and unstable [9, 10] cases, and obtained horizontal roll vortices only for a moderate wall heating. Later, Coleman [11] conducted DNS of the turbulent Ekman boundary layer with a high Reynolds number of Re_f = 1000 to estimate universal constants of the classical similarity theory [12, 13]. Here, Re_f is defined by

$$Re_f = \frac{GD}{\nu} = \frac{G}{\sqrt{\nu f/2}}, \qquad (1)$$

where G is the geostrophic wind velocity, f the Coriolis parameter and D the viscous Ekman layer depth $(= \sqrt{2\nu/f})$. Shingai *et al*. [14] employed a larger com-

* ***Corresponding author***: *Prof. Hiroshi Kawamura, Department of Mechanical Engineering, Tokyo University of Science, 2641 Yamazaki, Noda-shi, Chiba, 278-8510 Japan. E-mail: kawa@rs.noda.tus.ac.jp*

putational domain and found that a large turbulent structure in the region where the mean velocity reached its maximum. Shingai *et al*. [14] also observed the inertial oscillation in the upper region.

In the present study, we calculated DNSs of the neutrally stratified turbulent Ekman boundary layer at the higher Reynolds numbers of Re_f = 1140 and 1393, which have been enabled by use of the Earth Simulator. Our objective is to investigate Reynolds number dependence and the three-dimensional characteristics (such as turbulence structures) in the turbulent Ekman boundary layer. The Reynolds number attainable through DNS is, however, still much smaller than those of the actual PBL. The RANS plays an important role in the simulation of the PBL. Accordingly, we evaluate the eddy-viscosity model proposed by Blackadar [15, 16] to improve it based on the present results.

2. Simulated flow and numerical methods

A calculated flow field is the turbulent Ekman boundary layer of an incompressible viscous fluid over a smooth surface. The system is rotating about a vertical axis with an angular velocity $\boldsymbol{\Omega} = (0, 0, f/2)$.

The flow is driven by the combination of the horizontal pressure gradient and the Coriolis force. The configuration of the computational domain is given in Figure 1. The periodic boundary conditions are imposed in the streamwise (x) and spanwise (y) directions. The non-slip condition is adopted on the bottom surface, and the Neumann condition on the upper boundary.

The fundamental equations set are as follows:

$$\nabla \cdot \boldsymbol{u} = 0, \tag{2}$$

$$\frac{\partial \boldsymbol{u}}{\partial t} + (\boldsymbol{u} \cdot \nabla)\boldsymbol{u} + 2\boldsymbol{\Omega} \times \boldsymbol{u} = -\frac{1}{\rho}\nabla p + \nu \nabla^2 \boldsymbol{u}, \tag{3}$$

where ρ is the fluid density and p the pressure.

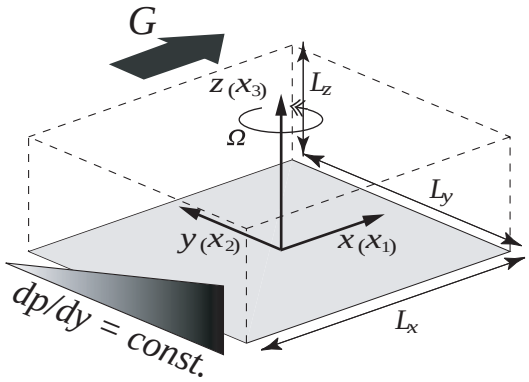

Fig. 1 Configuration of computational domain.

The fractional step method is used for the coupling between the continuity and the Navier-Stokes equations. The second-order Crank-Nicolson and the Adams-Bashforth methods are employed as the time advance algorithms; the former for the vertical viscous term and the latter for the other terms. The finite-different method is applied for the spatial discretization. The fourth-order central difference scheme [17] is adopted in the x- and y-directions, and the second-order central difference scheme in the wall-normal (z) direction.

The non-dimensional parameters are the Reynolds number (Re) and the Rossby number (Ro) defined by

$$Re = \frac{Gh}{\nu}, \quad Ro = \frac{G}{fh}, \tag{4}$$

where h is the height of the computational domain. Our calculations use these non-dimensional numbers as parameters, while those of Coleman *et al*. [7, 8, 9, 10, 11] used Reynolds number Re_f.

The summary of the computational conditions is given in Table 1. Here, L_x, L_y and L_z (= h) are the widths of the computational domain and N_x, N_y and N_z are the number

Table 1 Computational conditions.

Re_f	400	510	600	775	1140	1393
Re	8000	13000	18000	30000	65000	97000
Ro	10					
L_x, L_y	60.0D	102.0D	90.0D	147.2D	57.0D	90.5D
L_z	20.0D	25.5D	30.0D	38.7D	57.0D	69.6D
L_x^+, L_y^+	1560	3190	3200	6390	3384	6413
L_z^+	521	798	1060	1680	3384	4399
N_x, N_y	256	512	512	1024	512	1024
N_z	96	160	160	256	512	768
$\Delta x^+, \Delta y^+$	6.11	6.23	6.24	6.25	6.60	6.26
Δz^+	0.148–14.5	0.177–12.5	0.150–18.5	0.147–18.3	0.147–18.4	0.143–17.7
tf	90.0	43.0	57.0	15.7	23.3	4.3

of grid points in the x-, y- and z-directions, respectively. All variables with the superscript of + are normalized by ν and u_τ, where u_τ is the friction velocity. The computational domains of Re_f = 400, 510, 600, 775, 1140 and 1393 are bigger than the DNSs ever performed. The height of the computational domain is set such that it is large compared with the boundary layer thickness. The grid spacings Δ_x^+, Δ_y^+ and Δ_z^+ are decided based on the DNS of the turbulent Poiseuille flow performed by Abe *et al*. [18]. They reported that the results obtained by using the horizontal discretizations of $\Delta_x^+ = 8.00$ and $\Delta_y^+ = 5.00$ showed good agreement with the experimental data [19] and the results from the DNS with the spectral method [20]. As for the vertical spacing Δ_z^+, they used the non-uniform mesh in a range 0.15–8.02. In the present simulation, the horizontal grid spacing is almost of the same size as the spanwise spacing of Abe *et al*. [18], and the minimum value of the vertical spacing is nearly equal to the one used by them. Although the maximum value of the vertical spacing is about twice as large as the one of the Poiseuille flow, this is allowable because of the disappearance of small vortices in the upper region. As for the computational time, the averaging time is not enough in the case of Re_f = 1393. In this paper, therefore, we will present the data of only instantaneous flow fields with respect to the case of Re_f = 1393.

3. Reynolds number dependence of turbulence statistics

3.1 Mean velocity profile

The absolute values of mean velocity Q^+ as a function of the height z^+ are given in Figure 2 and compared with the experiments of Caldwell *et al*. [21]. The DNS of turbulent Ekman boundary layer performed by Coleman [11] and the one of the turbulent Poiseuille flow by Abe *et al*. [18] are also shown for comparison. The absolute velocity Q is defined as

$$Q = \sqrt{U^2 + V^2}, \tag{5}$$

where U and V are the streamwise and spanwise mean velocity components, respectively. The Reynolds number Re_L is defined by $Re_L = G/\sqrt{\nu\Omega_L}$, where Ω_L is the angular velocity of the plate rotation in the experiments of Caldwell *et al*. [21]. This Reynolds number is the same Reynolds number as Re_f by definition. The effect of rotation is only the Coriolis force in the present study, while the centrifugal force also takes place in their experiments. Even if Re_f is the same value of Re_L, some differences exist between the present study and his experiments. Thus, we use Re_L in the case of experiment to avoid confusion with our DNSs.

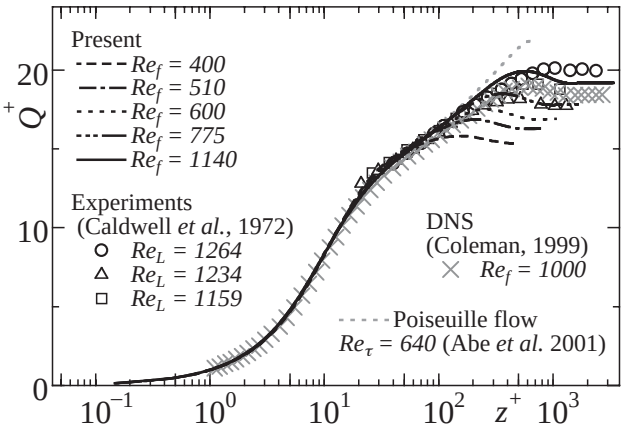

Fig. 2 Mean velocity profiles.

It is well known that the mean velocity follows the logarithmic region in wall turbulence, expressed as

$$Q^+ = \frac{1}{\kappa} \ln z^+ + C, \tag{6}$$

where κ is the von Kármán constant. Figure 2 shows that in the cases of Re_f = 400, 510 and 600, the logarithmic region is not observed due to the low Reynolds numbers. In the cases of Re_f = 775 and 1140, on the other hand, the logarithmic region starts to appear at $z^+ > 30$. Present results with Re_f = 775 and 1140 agree well with the experiments of Caldwell *et al*. [21] and with the DNS of Coleman [11].

The von Kármán constant κ can be obtained by

$$\frac{1}{\kappa} = z^+ \frac{dQ^+}{dz^+}. \tag{7}$$

The common value known for non-rotating turbulent boundary layers is κ = 0.4 – 0.42. The obtained results are shown in Figure 3. In the cases of Re_f = 400, 500 and 600, the von Kármán constant does not exhibit any constant region but increases monotonically. In the higher Reynolds number of Re_f = 775, κ starts to exhibit constant region. With the increasing Reynolds number, κ exhibits a local maximum and stays nearly at a constant value in a wider region. This trend is very close to the one obtained for the turbulent Poiseuille flow shown by a gray dotted line. This indicates that, if the mean velocity is expressed in the term of Q, the logarithmic nature of the mean velocity is very robust in spite of the three-dimensionality of the velocity field.

The hodographs of the mean velocities for Re_f = 400, 510, 600, 775 and 1140 are given in Figure 4. The analytical solution in the laminar Ekman boundary layer is also shown. The spiral shrinks as the increase of the Reynolds number. This means that the direction of the mean flow becomes closer to that of the geostrophic wind. The

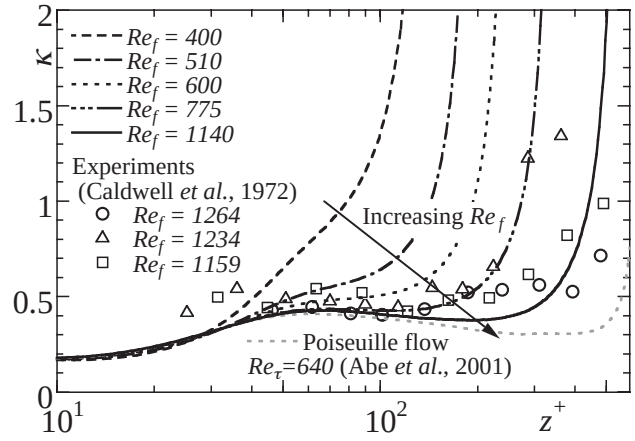

Fig. 3 von Kármán constants.

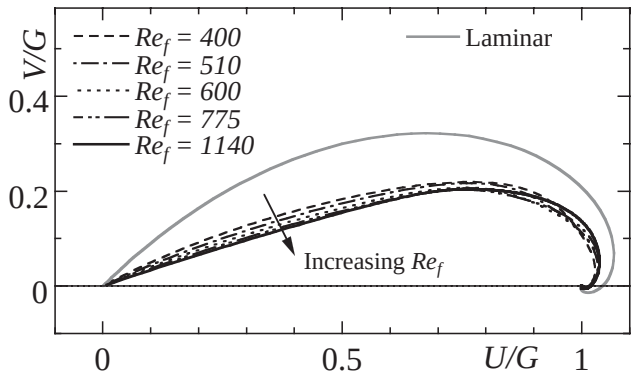

Fig. 4 Hodographs of mean velocities.

Table 2 Mean shear directions at the wall.

Re_f	400	510	600	775	1140
ϕ_{u0} [deg.]	28.7	25.4	23.3	21.2	19.4

angles ϕ_{u0} between the shear direction at the bottom wall and the geostrophic wind direction are shown in Table 2. The analytical solution of the laminar Ekman boundary layer gives 45 degrees. However, the angle ϕ_{u0} in the turbulent Ekman boundary layer decrease to a smaller value of 19 – 28 degrees. Caldwell *et al.* [21] also obtained the smaller angles of ϕ_{u0} = 19 – 28 in his experiments. As for the Reynolds number dependence, the angle ϕ_{u0} decreases with the increase of the Reynolds number. This is because the momentum transfer to the vertical direction is enhanced in the case of the higher Reynolds numbers. Therefore the momentum of the geostrophic wind penetrates more deeply into the near-wall region for the higher Reynolds numbers.

3.2 Turbulent intensity

Turbulent intensities are shown in Figure 5. The height z is normalized by the wall-unit and δ_{Qmax}, where δ_{Qmax} is the height at which Q becomes maximal. In the vicinity

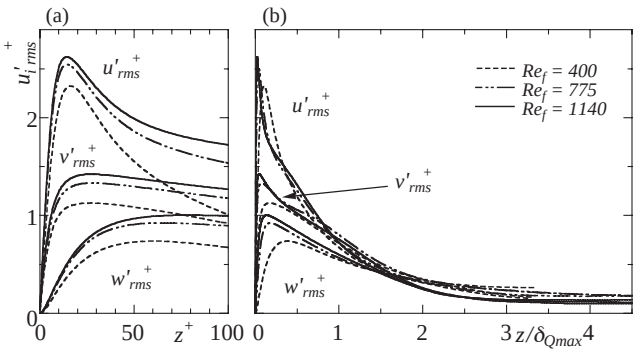

Fig. 5 Turbulent intensities as the function of z^+ (a) and z/δ_{Qmax} (b).

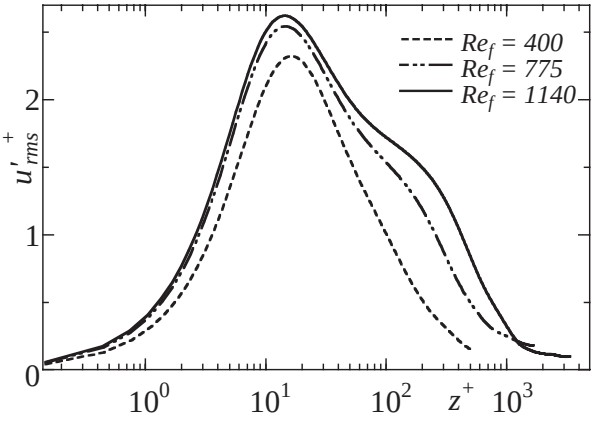

Fig. 6 Streamwise turbulent intensity.

of the wall, the velocity fluctuations of each component become larger with increasing the Reynolds number. In the upper region, on the other hand, the fluctuations are isotropic. Note that in the case of Re_f = 1140, the velocity fluctuations of each component at $z/\delta_{Qmax} > 1.5$ is smaller than those in the others Reynolds numbers. This is because the box size for Re_f = 1140 is smaller than the other cases. Figure 6 shows the streamwise velocity fluctuation ($u'_{\rm rms}$) plotted against z^+. It becomes larger in the logarithmic region (z^+~200) with increasing the Reynolds number. This trend is same as in turbulent channel and pipe flows. Morrison *et al.* [22] reported that the second maximum appeared for high Reynolds numbers.

3.3 Budget of Reynolds stress

For the turbulent Ekman boundary layer flows, the transport equations are given by

$$\frac{D}{Dt}\overline{u_i'u_j'} = P_{ij} + T_{ij} + \Pi_{ij} + D_{ij} + C_{ij} - \varepsilon_{ij}\,, \qquad (8)$$

where the terms on the right-hand side are identified as follows

production term:

$$P_{ij} = -\overline{u_j'u_k'}\,\frac{\partial U_i}{\partial x_k} - \overline{u_j'u_k'}\,\frac{\partial U_j}{\partial x_k},$$

turbulent diffusion term:

$$T_{ij} = -\frac{\partial}{\partial x_k}\overline{u_i' u_j' u_k'},$$

velocity pressure-gradient correlation term:

$$\Pi_{ij} = -\left(\overline{u_j'\frac{\partial p'}{\partial x_i}} + \overline{u_i'\frac{\partial p'}{\partial x_j}}\right),$$

molecular diffusion term:

$$D_{ij} = \nu\frac{\partial^2}{\partial x_k^2}\overline{u_i' u_j'},$$

Coriolis force production term:

$$C_{ij} = -\varepsilon_{ikl} f_k \overline{u_j' u_l'} - \varepsilon_{jkl} f_k \overline{u_i' u_l'},$$

dissipation term:

$$\varepsilon_{ij} = -2\nu\overline{\left(\frac{\partial u_i'}{\partial x_k}\right)\left(\frac{\partial u_j'}{\partial x_k}\right)},$$

where, ε in the Coriolis force production term is Eddington's epsilon. The indices (1, 2, 3) are used to denote the streamwise (x), spanwise (y) and wall-normal (z) directions, respectively.

Figure 7 shows the terms in the budget of $\overline{w'w'}$. The black and the red lines show the terms for Re_f = 400 and 1140, respectively. The Coriolis force production term C_{33} in the budget of $\overline{w'w'}$ is equal to zero. The values of Π_{33}, D_{33} and ε_{33} increase near the wall with the increasing Reynolds number. However, the profile of T_{33} at the low Reynolds number differs from that at the high Reynolds number. In the case of the low Reynolds number, T_{33} loses energy near the wall. On the other hand, in the case of the high Reynolds number T_{33} gains energy. Moreover, as the Reynolds number increases, the profile of T_{33} tends to be close to that of the turbulent Poiseuille flow (Figure 8). This means that the flow field in the vicinity of the wall becomes gradually two-dimensional turbulent flow with the increasing Reynolds number. Since the term T_{33} is expressed as $-\partial\left(\overline{w'w'w'}\right)/\partial z$, there is also difference in the skewness factor of w', i.e., S(w'). It should be noted that the profile of S(w') at $z^+ < 5$ in the Ekman boundary layer becomes more negative with the increasing Reynolds number (see Figure 9). This tendency does not correspond to that of the turbulent Poiseuille flow. In the fully developed Poiseuille flow, S(w') at the wall is positive (see the dotted light gray line in Figure 9). This means the so-called Q2 (ejection) event is less frequent but dominant in the u'–w' coordinate of the Poiseuille flow. On the other hand, in the case of the Ekman boundary layer, Q4 (sweep) event becomes more and more dominant with increasing Re_f. This is a new finding and the underlying reason is left of further study.

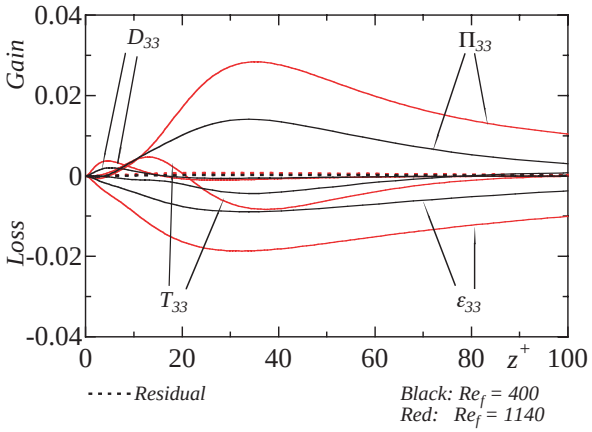

Fig. 7 Budget of $\overline{w'w'}$ normalized by u_τ^4/ν.

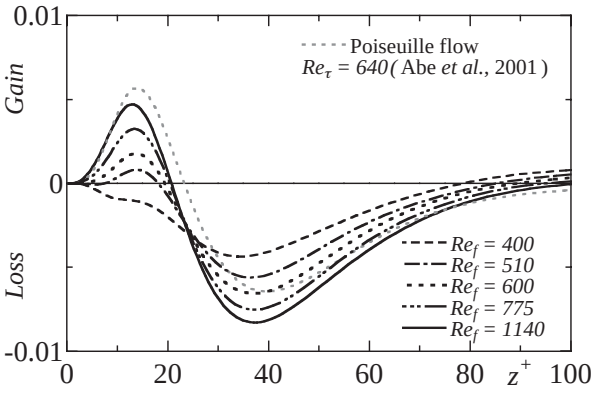

Fig. 8 Profile of T_{33} normalized by u_τ^4/ν.

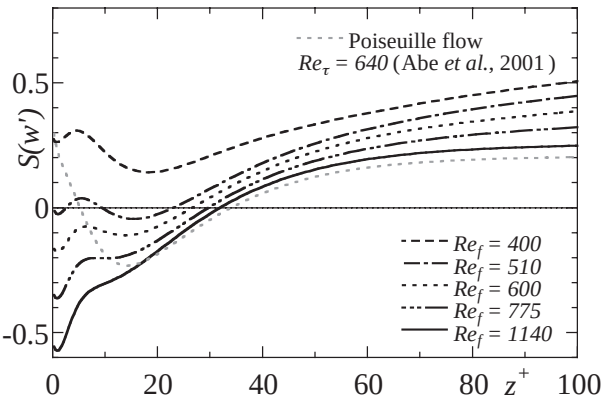

Fig. 9 Skewness factor $S(w')$.

For the budget of $\overline{v'v'}$, it is clear that the terms of T_{22}, P_{22}, D_{22} and ε_{22} are well scaled by the wall-unit (Figure 10). The profile of P_{22} ($=-2\overline{v'w'}\partial V/\partial z$) at the high Reynolds number, however, differ from that at the low Reynolds number as shown in Figure 11. The profile of P_{22} has two peaks at each Reynolds number. The first peak increases at $z^+ \sim 10$ with the increasing Reynolds number. This is because $-\overline{v'w'}$ decreases at $z^+ \sim 10$ with the increasing Reynolds number and $\partial V^+/\partial z^+$ varies little. On the other hand, the second peak decreases with the increasing Reynolds number. The point of the second

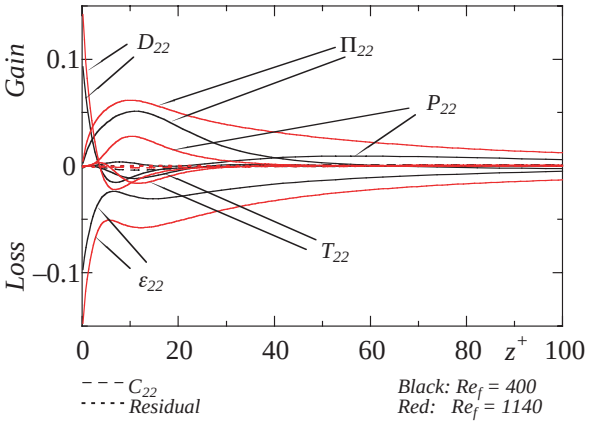

Fig. 10 Budget of $\overline{v'v'}$ normalized by u_τ^4/ν.

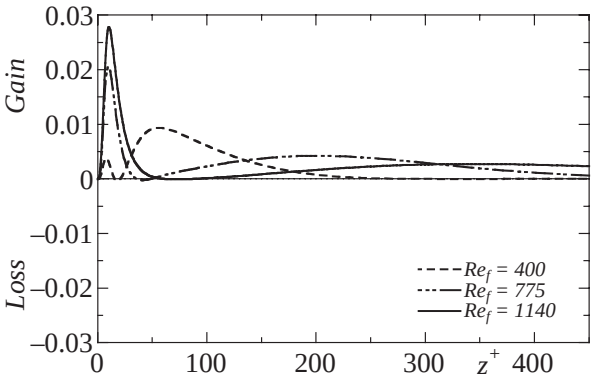

Fig. 11 Profile of P_{22} normalized by u_τ^4/ν as a function of z^+.

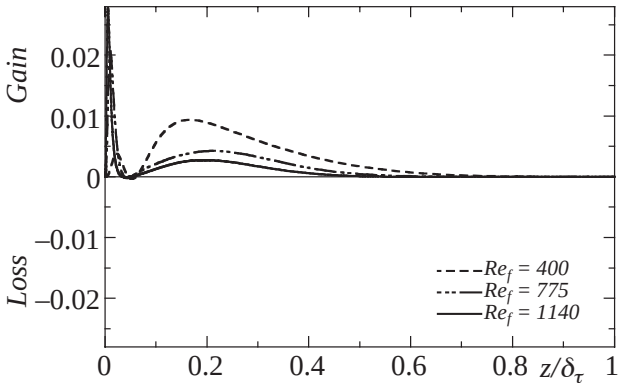

Fig. 12 Profile of P_{22} normalized by u_τ^4/ν as a function of z/δ_τ.

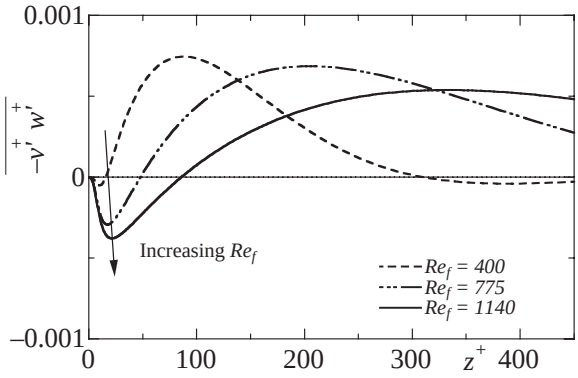

Fig. 13 Reynolds stress $-\overline{v'w'}$.

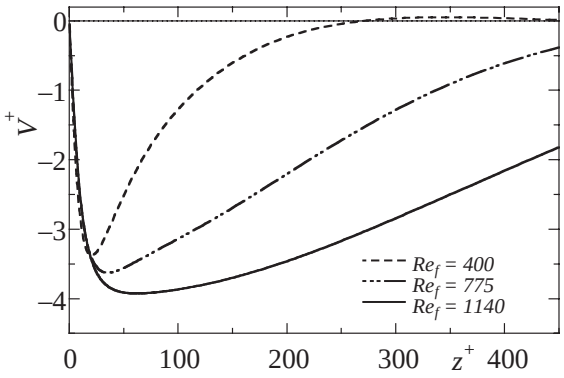

Fig. 14 Profile of spanwise mean velocity.

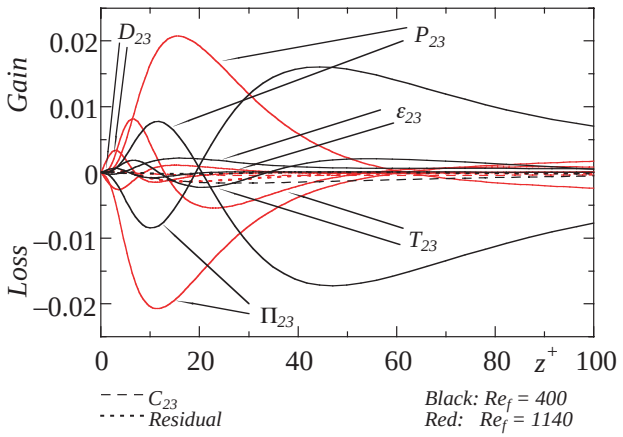

Fig. 15 Budget of $\overline{v'w'}$ normalized by u_τ^4/ν.

peak roughly corresponds to the maximum of $-\overline{v'w'}$ and it's value decreases at the high Reynolds number (Figure 13). On the contrary, $\partial V^+/\partial z^+$ at the high Reynolds number decreases at that point (Figure 14). The second peak at the high Reynolds number consequently decreases. In addition, for the second peak of P_{22} is well scaled by δ_τ (Figure 12), where δ_τ (= u_τ/f) is the turbulent depth. This indicates that P_{22} is affected by the outer region.

Figure 15 shows the budget of $\overline{v'w'}$. The term of P_{23} ($=-\overline{w'w'}\partial V/\partial z$) denotes the same tendency of P_{22}. The first peak increases at $z^+ \sim 15$ with the increasing Reynolds number, while the second peak decreases as shown in Figure 16. This is because $\overline{w'w'}$ increases at $z^+ \sim 10$ with the increasing Reynolds numbers while $\partial V^+/\partial z^+$ varies little at that height (Figure 18). In addition, the second peak of P_{23} roughly corresponds to the maximum point of the spanwise mean velocity gradient. In the case of the low Reynolds number, its gradient is larger. Thus the first peak of P_{23} is larger and the second peak decreases with the increasing Reynolds number. Moreover, the second peak of P_{23} is well scaled by the outer variables (Figure 17). This tendency is also seen in P_{22}.

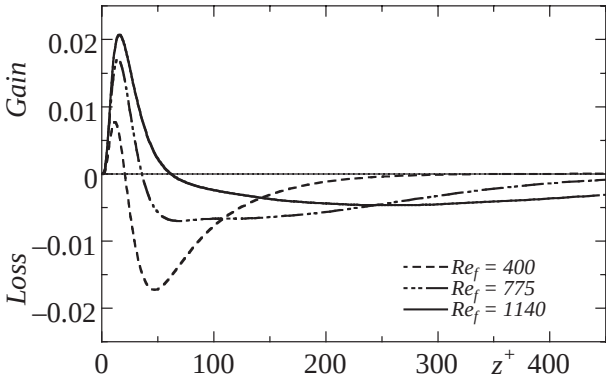

Fig. 16 Profile of P_{23} normalized by u_τ^4/ν as a function of z^+.

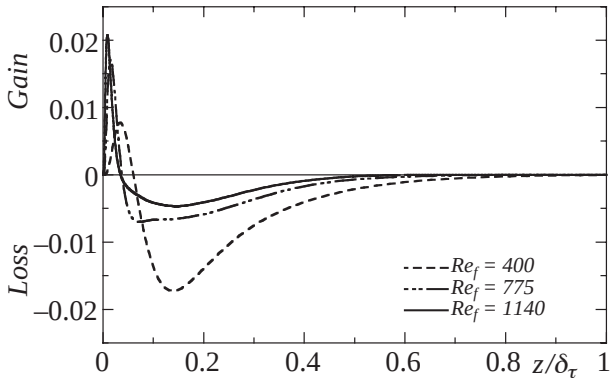

Fig. 17 Profile of P_{23} normalized by u_τ^4/ν as a function of z/δ_τ.

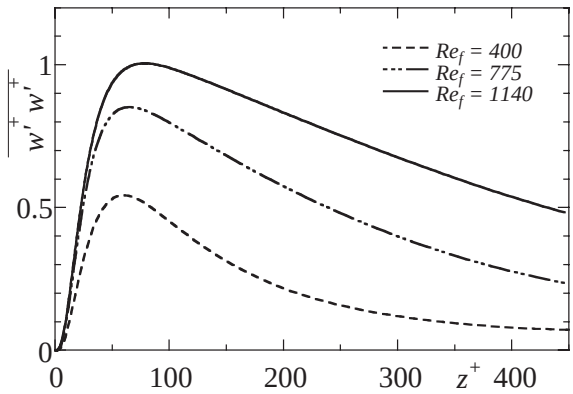

Fig. 18 Profile of $\overline{w'w'}^+$.

4. Turbulence structure

4.1 Large-scale structure

Figure 19 shows the spanwise wavelength λ_y of the maxima of the pre-multiplied energy spectra for each Reynolds number. It is well known that the wavelength at the peak of the pre-multiplied energy spectrum indicates that of the mainly energy-containing scale (MES). In the vicinity of the wall, the spanwise wavelength of MES is $\lambda_y^+ \sim 100$. This corresponds to the streaky structures near the wall. In the mid-height region ($z/D < 6$), the length scales increase linearly with the increasing height. In the upper region ($6 < z/D < 15$), however, the wavelengths of

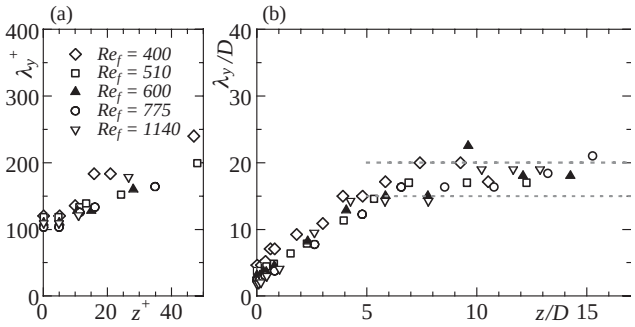

Fig. 19 Spanwise wavelength of the maxima of the pre-multiplied spectra normalized by (a) the wall-unit and (b) the viscous Ekman depth D.

MES stay at a constant value of $\lambda_y/D \sim 15$–20. This suggests the existence of the large-scale structures which can be scaled spanwisely by the viscous Ekman layer depth D. In the former study, Shingai *et al*. [14] suggested the spanwise wavelength of MES can be scaled by δ_{Qmax}. The present study, however, indicates that the scaling by the viscous Ekman layer depth gives a better collapse.

A y–z plane view of an instantaneous flow field at each Reynolds number is visualized in Figure 20. The contours show the strength of the instantaneous streamwise velocity fluctuations u'^+. The red and the blue regions represent the high- and low-speed regions, respectively. In the near-wall region, the small-scale structures are observed, while the scale of structures increases linearly with the increasing height. This result is in accordance with that of Figure 19. These figures also indicate that the structures of about $15D$–$20D$ scale exist at $z/D \sim 6$ for each Reynolds number. It should be noted that these large-scale structures incline toward the y-direction. Since these structures are not observed in the channel flow, it is a particular structure of the Ekman boundary layer.

To grasp the three-dimensional characteristics of the turbulence structures, a bird's eye view of an instantaneous flow field for $Re_f = 1393$ is displayed in Figure 21. Figure 22 is an enlarged view of a part of Figure 21 from a different view point. The isosurfaces, colored red and blue, show the high ($u'^+ > 3.0$)- and low ($u'^+ < –3.0$)-speed regions, respectively. The green isosurfaces show the low-speed regions ($u'^+ < –1.2$) at $z/D > 5$. The streaky structures are observed near the wall and elongated along the mean velocity direction. On the other hand, large low-speed regions exist in the upper region. The large-scale structures rise up from the bottom because the low-speed fluid is conveyed from the bottom wall. The structures are not aligned in the direction of the mean velocity. They are elongated approximately in the direction of the geostrophic wind (in the x-direction) and are also inclined slightly toward the higher pressure side (in the minus y-

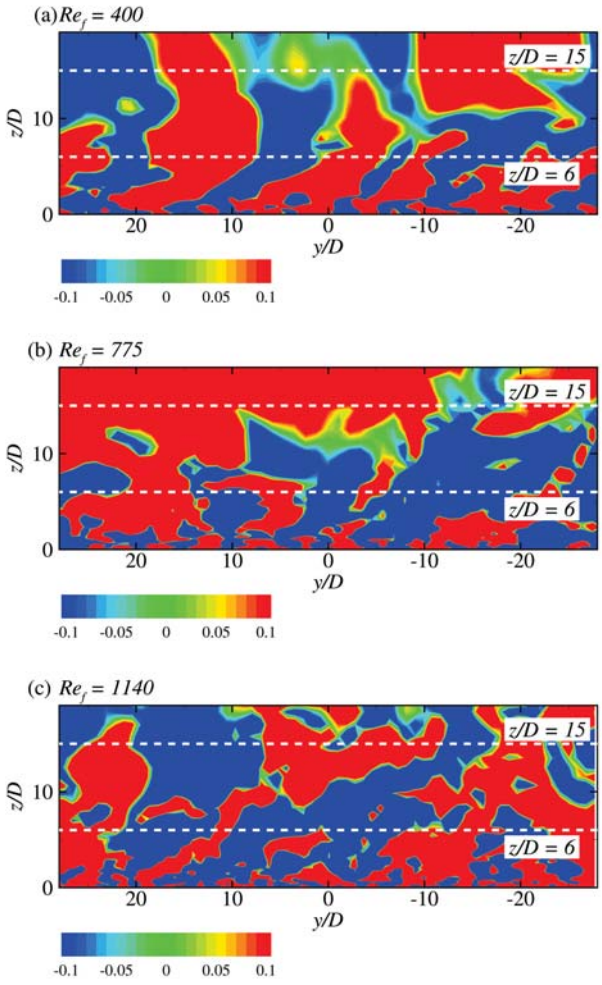

Fig. 20 Contours of instantaneous flow field in the *y*-*z* plane for Re_f = 400, 775 and 1140.

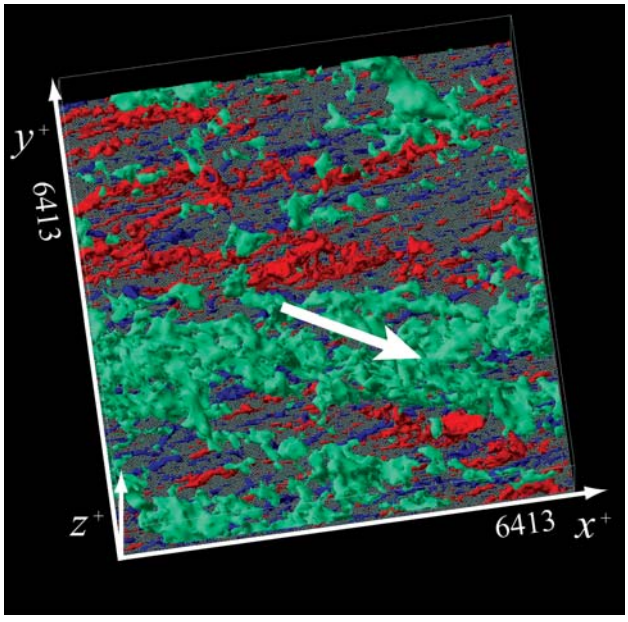

Fig. 21 Bird's eye view of instantaneous flow field for Re_f = 1393. Red: high-speed regions $u'^+ > 3.0$; blue: low-speed regions $u'^+ < -3.0$; green: low-speed regions in the upper region $u'^+ < -1.2$ at $z/D > 5$.

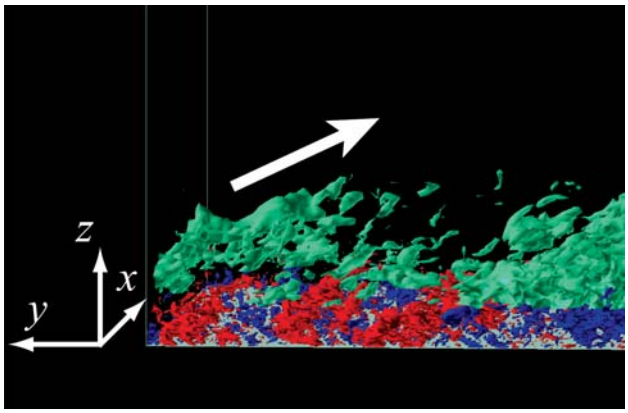

Fig. 22 Enlarged view of a part of Figure 21 from a different view point.

direction). We examine the inclination of these large-scale structures in more detail in the next section.

4.2 Material line

To examine the large-scale structure circumstantially, the motions of passive material lines in the turbulent Ekman boundary layer are visualized. Batchelor [23], Kida *et al*. [24] and Goto *et al*. [25] studied material lines in turbulent flows. They focused mainly upon the stretching rates of material lines.

The material line is represented by a chain which consists of fluid particles. An arbitrary point on the material line is advected by the local velocity as

$$\frac{dx_p(t)}{dt} = \boldsymbol{u}(\boldsymbol{x}_p(t),(t)), \tag{9}$$

where the suffix p is an index of the particles. The term on the right-hand side of equation (9) is calculated by linear interpolation in terms of the velocity field at the grid points. The perfect elastic collision condition is adopted on the bottom wall. Although the same condition is assumed to the top boundary condition, no particle has reached the top boundary. The segments of the material line are generally elongated as time elapses. Whenever the distance between the adjacent two particles reaches a half of the spanwise grid spacing Δz, a new particle is inserted at the center between the two particles. The maximal total number of particles is limited due to the computational resource.

In order to evaluate an effect of the initial distance from the wall, the material lines are released at z^+ = 17 (z/D = 0.65) and z^+ = 152 (z/D = 5.85) (see Figure 23(a)). The length of each material line is the half of the spanwise box size. Snapshots of the material lines at four time instants for Re_f = 400 are drawn in Figure 23. In the vicinity of the wall, the material line becomes wavy and is elongated toward the lower pressure with time. This corresponds to

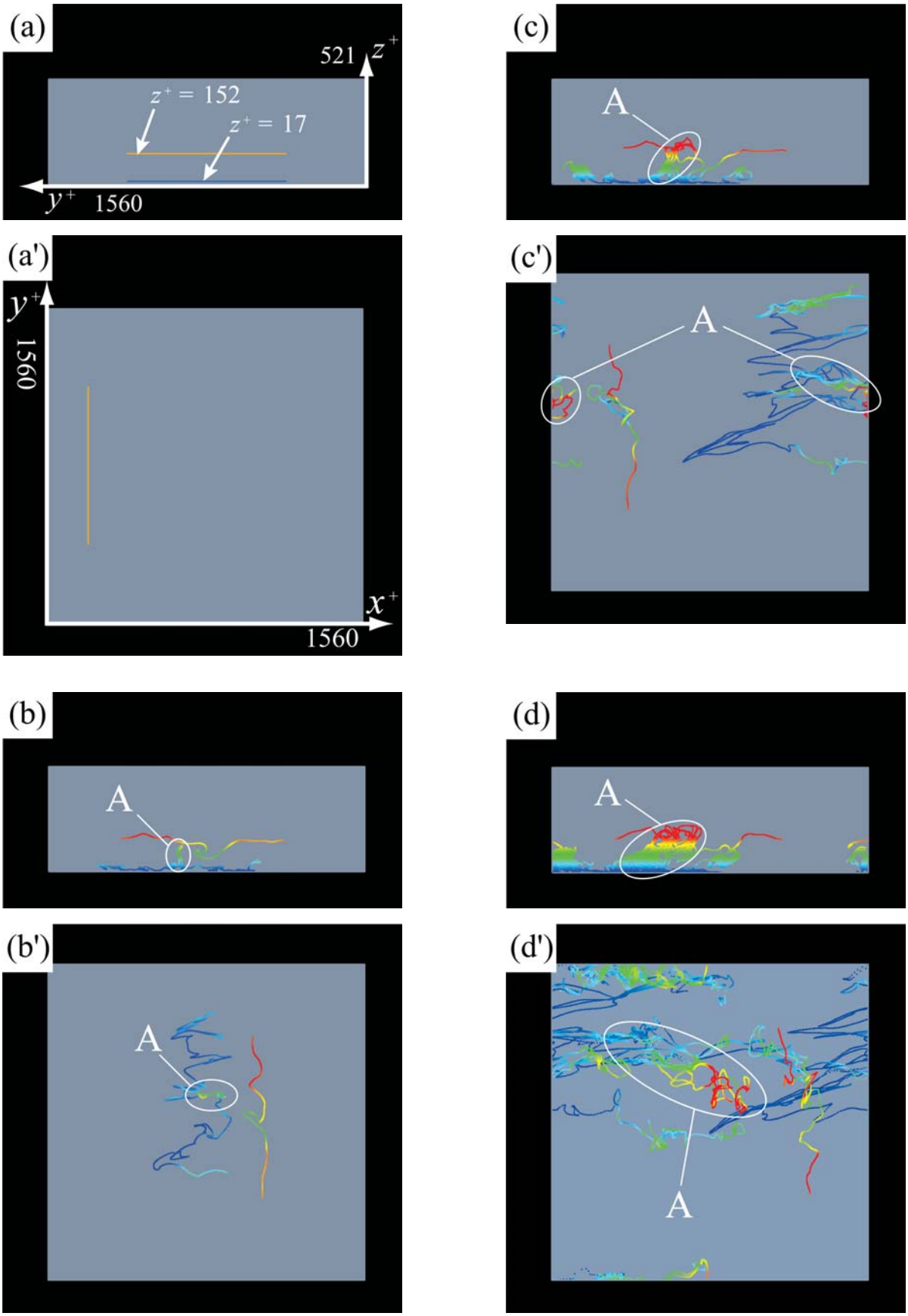

Fig. 23 Motions of material line for $Re_f = 400$. a'–d' are the top views, while a–d are the side views seen from the left of a'–d'. The color indicates the height from the bottom wall blue to red, $z^+ = 0$ to $z^+ = 182$ ($z/D = 7$). (a, a') $t^+ = 0$, (b, b') $t^+ = 54$, (c, c') $t^+ = 108$, (d, d') $t^+ = 162$.

the streaky structure in Figure 21. A strong ejection event is observed in the oval A in Figure 23. If we compare between the advected spanwise distance for the material line raised up to the outer region and the one staying in the vicinity of the wall, the distance of the former one is smaller than that of the latter. This is because the spanwise mean velocity V is larger in the vicinity of the wall than in the outer region. In fact, the spanwise movement of the material line near the wall in the oval A is roughly equal to the product of the spanwise mean velocity V and the elapsed time t^+. Therefore, the inclination of the large-scale structure as described in the previous sub-section is cased by the combination of the strong ejection and the three-dimensional mean velocity profile.

5. Eddy-viscosity model

Many theoretical approaches to the turbulent Ekman problem have employed some empirical specification for the eddy-viscosity. Among them, we will examine a mixing length model proposed by Blackadar [15, 16] in comparison with the present DNS data. The eddy-viscosity coefficient is generally defined by

$$-\overline{u'w'} = K_m \frac{dU}{dz}, \quad -\overline{v'w'} = K_m \frac{dV}{dz}. \tag{10}$$

In the mixing length representation, the eddy-viscosity is expressed as

$$K_m = l^2 S \tag{11}$$

where l is the mixing length defined later and S the magnitude of the wind shear

$$S = \left\{ \left(\frac{dU}{dz} \right)^2 + \left(\frac{dV}{dz} \right)^2 \right\}^{\frac{1}{2}}. \tag{12}$$

The mixing length l in equation (11) is assumed to have a form

$$\frac{1}{l} = \frac{1}{\kappa z} + \frac{1}{\lambda}. \tag{13}$$

Here, λ is an empirical parameter which specifies a maximum value of l as z approaches infinity. Blackadar [15] first used the following empirical relation for λ:

$$\lambda = 2.7 \times 10^{-4} \frac{G}{f}, \tag{14}$$

while in his later paper [16] he used the relation

$$\lambda = u_\tau \frac{H}{G}, \tag{15}$$

where H is the boundary layer thickness and u_τ the friction velocity. We used equation (15) for λ to compare with our DNS data and calculated u_τ and H from DNS data. Here, H is assumed the height at which the wind direction becomes first parallel to the geostrophic wind direction.

For the case of a steady state $\left(\partial \overline{(\ )}/\partial t = 0\right)$ and horizontally homogeneous state $\left(\partial \overline{(\ )}/\partial x = 0,\ \partial \overline{(\ )}/\partial y = 0\right)$, the Navier-Stokes equation (3) with the assumed eddy-viscosity model of equation (11) can be expressed as

$$\frac{d}{dz}\left\{ (\nu + K_m) \frac{dU}{dz} \right\} = -fV, \tag{16}$$

$$\frac{d}{dz}\left\{ (\nu + K_m) \frac{dV}{dz} \right\} = -f(U - G), \tag{17}$$

These equations were solved numerically. The bottom and top boundary conditions are $U = 0$, $V = 0$ and $U = G$, $V = 0$, respectively. Figure 24 shows the eddy-viscosity profiles. The dashed lines show the results by the

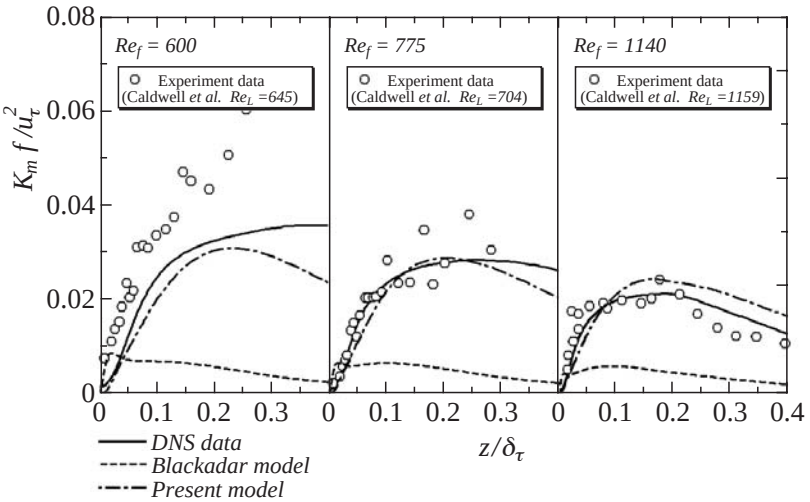

Fig. 24 Eddy-viscosity profiles.

Blackadar's model. The solid lines show the viscosity profiles derived from mean velocity profiles of our DNS. The eddy viscosity derived from our DNS data is calculated by the formula:

$$K_m(z) = \left(\tau_x^2 + \tau_y^2\right)^{\frac{1}{2}} \left\{ \left(\frac{dU}{dz}\right)^2 + \left(\frac{dV}{dz}\right)^2 \right\}^{-\frac{1}{2}}. \quad (18)$$

The calculation of K_m requires the mean velocity gradients. The Blackadar's model does not agree with DNS data at all the Reynolds numbers tested. In the vicinity of the wall, the results of the Blackadar's model are larger than our results. This is because the effect of viscosity is not considered in equation (13). In the rest of the part, the eddy-viscosity profiles using Blackadar's model are smaller. The mixing length profiles are shown in Figure 25 and compared with the experiments of Caldwell *et al.* [21]. The mixing length can be computed by applying the following definition:

$$l(z) = \left(\tau_x^2 + \tau_y^2\right)^{\frac{1}{4}} \left\{ \left(\frac{dU}{dz}\right)^2 + \left(\frac{dV}{dz}\right)^2 \right\}^{-\frac{1}{2}}. \quad (19)$$

The mixing lengths by the experiment and the DNS agree almost well with each other. A discrepancy increases with the increasing height. This is because the mean velocity gradients become smaller at the larger height, thus the derivation of l becomes less accurate in the experiment. The Blackadar's model does not agree with our DNS data for all the calculated Reynolds numbers in spite that the accurate magnitude S of the wind shear is used for the model, too. To reduce the discrepancy, we will introduce the viscous effect in the near wall region and will accommodate an empirical parameter λ relevant to the upper region. The van Driest damping function is employed to express the viscous effect while in the upper region the mixing length is assumed to be proportional to the viscous Ekman depth D. Accordingly, a newly defined l and λ becomes

$$\frac{1}{l} = \frac{1}{\kappa z\{1 - \exp(-z^+/A^+)\}} + \frac{1}{\lambda}, \quad (20)$$

$$\lambda = C_\lambda D, \quad (21)$$

where A^+ and C_λ are model constants. In this paper, these model constants are set to be $A^+ = 26\left\{1 + (290/Re_f)^2\right\}$ and C_λ = 2.0. The results of the present model are shown in Figures 24 and 25 by the dotted-and-dashed lines. The present model is in better agreement with our DNS data than the Blackadar's one. The mean velocity profiles calculated from the Blackadar's model and the present one are compared in Figures 26 and 27 with the DNS data. The present model predicts the mean velocity profiles give a much better agreement with the DNS data. Table 3 shows the angle ϕ_{u0} and u_τ calculated from DNS, the Blackadar's and the present models. The Blackadar theory doesn't predict both ϕ_{u0} and u_τ. On the other hand, the present model gives very close values to those of the DNS data.

6. Conclusion

We have performed direct numerical simulations of the turbulent Ekman boundary layer over a smooth surface. The Reynolds numbers Re_f were 400, 510, 600, 775, 1140 and 1393 in order to investigate Reynolds number dependence. The three-dimensional characteristics in the turbulent Ekman boundary layer flow were studied. In addition, we evaluated the existing eddy-viscosity model [15, 16], and proposed an improved modeling. The derived conclusions are as follows:

1. The logarithmic region appears more clearly in the

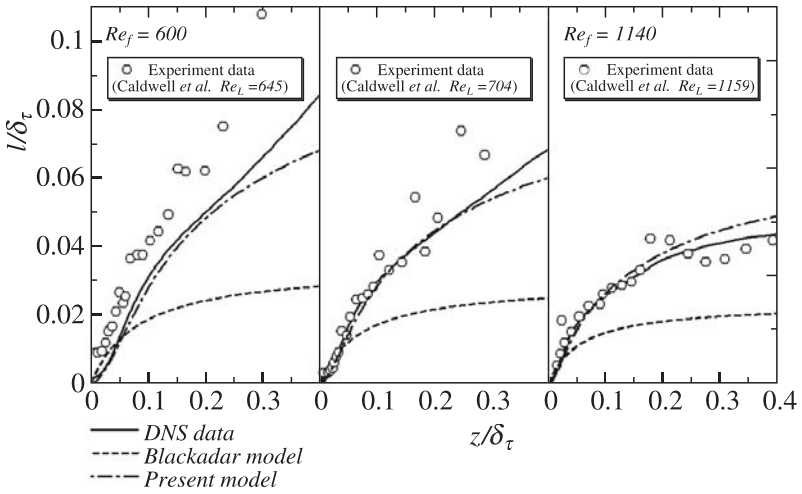

Fig. 25 Mixing length profiles.

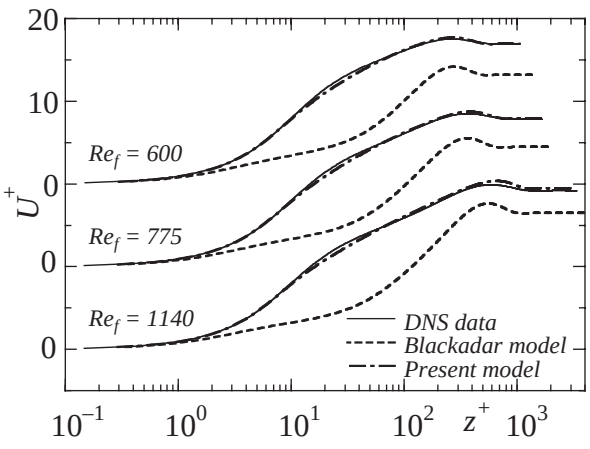

Fig. 26 Streamwise mean velocity profiles.

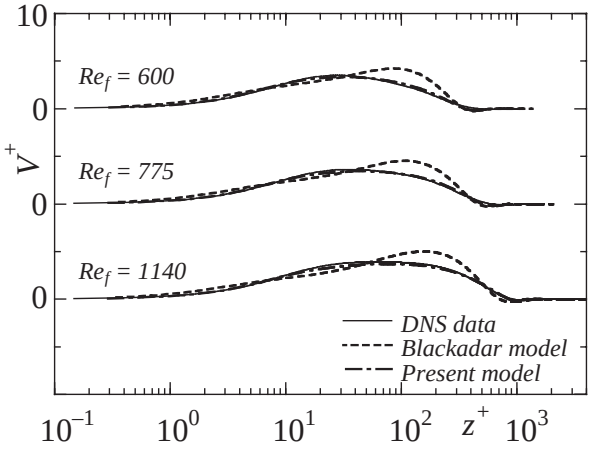

Fig. 27 Spanwise mean velocity profiles.

Table 3 Comparisons with eddy-viscosity models.

	DNS		Blackadar model		Present model	
Re_f	u_τ/G	ϕ_{u0} [deg.]	u_τ/G	ϕ_{u0} [deg.]	u_τ/G	ϕ_{u0} [deg.]
600	0.0592	23.3	0.0757	36.7	0.0590	24.1
775	0.0561	21.2	0.0691	36.3	0.0557	21.9
1140	0.0521	19.4	0.0607	35.3	0.0513	19.7

higher Reynolds number cases of Re_f = 775 and 1140. The results of Re_f = 775 and 1140 agree well with the results of experiment by Caldwell *et al.*. In the higher Reynolds numbers of Re_f = 775 and 1140, the von Kármán constant κ starts to exhibit a constant region. Moreover, with increasing the Reynolds number, κ exhibits a local maximum and nearly stays nearly at a constant value in a wider region.

2. The Reynolds number dependence of the terms of T_{33}, P_{22} and P_{23} is significant. The turbulent diffusion T_{33} at the high Reynolds number tends to be close to the profile of the Poiseuille flow in the vicinity of the wall. This means that the flow field near the wall becomes gradually two-dimensional with the increasing Reynolds number. However, the profiles of the skewness factor S(w') at high Reynolds number differ from that of the Poiseuille flow. The profile of S(w') at $z^+ <$ 5 in the Ekman boundary layer becomes more negative with the increasing Reynolds number. This means the sweep event becomes more dominant in the Ekman boundary layer.
3. The analysis using the pre-multiplied energy spectra and instantaneous flow fields in y–z plane indicates that the large-scale structures with a spanwise scale of 15D–20D exist in the upper region (z/D ~ 6). In addition, it is found that the low-speed large-scale structures are not aligned in the direction of the mean velocity. They are elongated approximately in the direction of the geostrophic wind and also slightly toward the higher pressure side. The motion of material lines reveals the mechanism of the inclination of the large-scale structures. That is, the inclination of the large-scale structure is cased by the combination of the strong ejection event and the three-dimensional mean velocity profile.
4. The existing model does not show good agreement with our DNS data. An improvement is proposed to the expression of the mixing length. The mean velocity profiles calculated from our improved model well agree with our DNS data.

Acknowledgments

The present calculations of higher Reynolds numbers were carried out by using the Earth Simulator at Japan Agency for Marine-Earth Science and Technology. We would heartily appreciate the performance of the computations and also helpful technical supports by the staffs Mr. H. Murai and Y. Tuda. The present research was made as an activity of Turbulence Research Forum leaded by Prof. C. Arakawa of the University of Tokyo. Calculations of smaller Reynolds numbers were carried out at VPP5000/64 at the Computing and Communications Center, Kyushu University and SX-7 at the Information Synergy Center, Tohoku University.

(This article is reviewed by Dr. Tetsuya Sato.)

References

[1] C. -H. Moeng, A large-eddy-simulation model for the study of planetary boundary layer turbulence, *J. Atmos. Sci*., vol.**41**, no.13, pp.2052–2062, 1984.

[2] P. J. Mason, Large-eddy simulation of the convective atmospheric boundary layer, *J. Atmos. Sci*., vol.**46**, no.11, pp.1492–1516, 1989.

[3] A. Andrén, and C.-H. Moeng, Single-point closures in a neutrally stratified boundary layer, *J. Atmos. Sci*., vol.**50**, no.20, pp.3366–3379, 1993.

[4] C. -L. Lin, J. C. Mcwilliams, C. -H. Moeng, and P. P. Sullivan, Coherent structures and dynamics in a neutrally stratified planetary boundary layer flow, *Phys. Fluids*, vol.**8**, no.10, pp.2626–2639, 1996.

[5] P. G. Duynkerke, Application of the E-ε turbulence closure model to the neutral and stable atmospheric boundary layer, *J. Atmos. Sci*., vol.**45**, no.5, pp.865–880, 1988.

[6] A. Andrén, A TKE-dissipation model for the atmospheric boundary layer, *Boundary-Layer Meteorol*., vol.**56**, pp.207–221, 1991.

[7] G. N. Coleman, J. H. Ferziger, and P. R. Spalart, A numerical study of the turbulent Ekman layer, *J. Fluid Mech*., vol.**213**, pp.313–348, 1990.

[8] G. N. Coleman, J. H. Ferziger, and P. R. Spalart, Direct simulation of the stable stratified turbulent Ekman layer, *J. Fluid Mech*., vol.**244**, pp.677–712, 1992.

[9] G. N. Coleman, J. H. Ferziger, and P. R. Spalart, A numerical study of the convective boundary layer, *Boundary-Layer Meteorol*., vol.**70**, pp.247–272, 1994.

[10] G. N. Coleman, and J. H. Ferziger, Direct numerical simulation of a vigorously heated low Reynolds number convective boundary layer, *Dyn, Atmos. Oceans*, vol.**24**, pp.85–94, 1996.

[11] G. N. Coleman, Similarity of statistics from a direct numerical simulation of the neutrally stratified planetary boundary layer, *J. Atmos. Sci*., vol.**56**, pp.891–900, 1999.

[12] G. T. Csanady, On the 'resistance law' of a turbulent Ekman layer, *J. Atmos. Sci*., vol.**24**, pp.467–471, 1967.

[13] P. R. Spalart, Theoretical and numerical study of a three-dimensional turbulent boundary layer, *J. Fluid Mech*., vol.**205**, pp.319–340, 1989.

[14] K. Shingai, and H. Kawamura, A study of turbulent structure and large-scale motion in the Ekman layer through direct numerical simulations, *J. Turbulence*, vol.**5**, no.13, 2004.

[15] A. K. Blackadar, The vertical distribution of wind and turbulent exchange in a neutral atmosphere, *J. Geophys. Res*., vol.**67**, no.8, pp.3095–3102, 1962.

[16] A. K. Blackadar, A single-layer theory of the vertical distribution of wind in a baroclinic neutral atmospheric boundary layer, *Final Rept. AFCRL-65-531*, Department of Meteorology, Pennsylvania State University, pp.22, 1965.

[17] Y. Morinishi, Conservative properties of finite difference scheme for in compressible flow, *CTR Annual Research Briefs*, pp.121–132.

[18] H. Abe, H. Kawamura, and Y. Matsuo, Direct numerical simulation of fully developed turbulent channel flow with respect to the Reynoles number dependence, *Trans. ASME J. Fluids Eng*., vol.**123**, pp.382–393, 2001.

[19] A. K. M. F. Hussain, and W. C. Reynolds, Measurements in fully developed turbulent channel flow, *Trans. ASME J. Fluids Eng*., vol.**97**, pp.568–580, 1975.

[20] R. D. Moser, J. Kim, and N. N. Mansour, Direct numerical simulation of turbulent channel flow up to Re_τ = 590, *Phys. Fluids*, vol.**11**, pp.943–945, 1999.

[21] D. R. Caldwell, C. W. Van Atta, and K. N. Helland, A laboratory stury of the turbulent Ekman layer, *Geophys. Fluid Dyn*., vol.**3**, pp.125–160, 1972.

[22] J. F. Morrison, B. J. Mckeon, W. Jiang, and A. J. Smits, Scaling of the streamwise velocity component in turbulent pipe flow, *J. Fluid Mech*., vol.**508**, pp.99–131, 2004.

[23] G. K. Batchelor, The effect of homogeneous turbulence on material lines and surfaces, *Proc. Roy. Soc. London Ser. A*, vol.**213**, pp.349–366, 1952.

[24] S. Kida, and S. Goto, Line statistics: Streching rate of passive lines in turbulence, *Phys. Fluids*, vol.**14**, pp.352–361, 2002.

[25] S. Goto, and S. Kida, A multiplicative process of material line stretching by turbulence, *J. Turbulence*, vol.**3**, no.17, 2002.